Article

Promoting Interfacial Interactions with the Addition of Lignin in Poly(Lactic Acid) Hybrid Nanocomposites

Bindu Patanair [1] , Allisson Saiter-Fourcin [1] , Sabu Thomas [2],*, Martin George Thomas [2],
Poornima Parathukkamparambil Pundarikashan [3], Kalaprasad Gopalan Nair [3], Varsha Krishna Kumar [4],
Hanna J. Maria [2] and Nicolas Delpouve [1],*

[1] Normandie Univ, UNIROUEN, INSA Rouen, CNRS, GPM, 76000 Rouen, France;
    bindu_patanair@yahoo.com (B.P.); allison.saiter@univ-rouen.fr (A.S.-F.)
[2] School of Chemical Sciences, School of Energy Materials and International and Inter-University Centre for
    Nanoscience and Nanotechnology, Mahatma Gandhi University, Priyadarshini Hills P.O, Kottayam,
    Kerala 686 560, India; martinpsrt@gmail.com (M.G.T.); hannavidhu@gmail.com (H.J.M.)
[3] Sree Narayana College, Nattika, Affiliated to the University of Calicut, Kerala 680 566, India;
    poornimapp1995@gmail.com (P.P.P.); gkalaprasad@gmail.com (K.G.N.)
[4] Majlis Arts and Science College Puramannur, Malappuram Dist, Kerala 676 552, India;
    varshakrishnavinz@gmail.com
* Correspondence: sabuthomas@mgu.ac.in (S.T.); nicolas.delpouve1@univ-rouen.fr (N.D.);
    Tel.: +91-9447223452 (S.T.); +33-(0)232955165 (N.D.)

Abstract: In this paper, the calorimetric response of the amorphous phase was examined in hybrid nanocomposites which were prepared thanks to a facile synthetic route, by adding reduced graphene oxide (rGO), Cloisite 30B (C30B), or multiwalled carbon nanotubes (MWCNT) to lignin-filled poly(lactic acid) (PLA). The dispersion of both lignin and nanofillers was successful, according to a field-emission scanning-electron microscopy (FESEM) analysis. Lignin alone essentially acted as a crystallization retardant for PLA, and the nanocomposites shared this feature, except when MWCNT was used as nanofiller. All systems exhibiting a curtailed crystallization also showed better thermal stability than neat PLA, as assessed from thermogravimetric measurements. As a consequence of favorable interactions between the PLA matrix, lignin, and the nanofillers, homogeneous dispersion or exfoliation was assumed in amorphous samples from the increase of the cooperative rearranging region (CRR) size, being even more remarkable when increasing the lignin content. The amorphous nanocomposites showed a signature of successful filler inclusion, since no rigid amorphous fraction (RAF) was reported at the filler/matrix interface. Finally, the nanocomposites were crystallized up to their maximum extent from the glassy state in nonisothermal conditions. Despite similar degrees of crystallinity and RAF, significant variations in the CRR size were observed among samples, revealing different levels of mobility constraining in the amorphous phase, probably linked to a filler-dimension dependence of space filling.

Keywords: PLA; CNT; rGO; MMT; glass transition; crystallization; morphology; thermal stability; calorimetry; cooperativity

1. Introduction

The bio-renewability, ease of processing, and suitability for mechanical recycling [1], as well as decent mechanical properties, make poly(lactic acid) (PLA) among the best substitutes to polymers derived from petroleum sources [2]. However, PLA has certain drawbacks, such as a small elongation at break (<10%), poor impact strength (~5 kJ m^{-2}), low heat-deflection temperature (<60 °C), and poor UV-light barrier properties [3]. Blending PLA with either other polymers or nanofillers offers more opportunities to tailor its properties. For instance, PP/PLA-blend nanocomposites with multiwalled carbon nanotubes (MWCNT) [4] have enhanced tensile strength and electrical conductivity. Hybrid

nanocomposites of PLA with nanocellulose/nanoclay have enhanced barrier properties and improved thermo-mechanical properties [5]. More specifically, nanocomposites, including nucleophilic nanofillers like nanoclay, graphene oxide (GO), and MWCNT, in PLA exhibit better protection against UV radiation [6], improved Young's modulus, antibacterial activity, potential use in biomedical applications [7], and increased thermal conductivity, as well as mechanical and electrical properties [8].

Lignin, one of the most abundant bio-macromolecules on earth, is biodegradable, nontoxic, and low-cost. Commercially, it is usually easily obtained as a byproduct in the pulp and paper industry. Its use is also regularly reported in biorefineries [9–11] and in carbon-fiber manufacturing [12,13]. Moreover, it exhibits interesting mechanical properties and decent thermal resistance. Hence, there is an increased amount of research on the use of lignin as a biomaterial [14–21]. Additionally, lignin has been used as an adhesion promoter in PLA/cotton-fiber composites [22]. The possibility of improving interfacial adhesion thanks to lignin is the consequence of the numerous intermolecular bonds it can be involved in. Therefore, it is possible to associate it in hybrid nanocomposites with PLA via interactions with nanofillers like MWCNT, reduced graphene oxide (rGO), and Cloisite 30B (C30B), which is an organically-modified montmorillonite nanoclay.

Whilst the nanocomposite morphology has been widely probed by X-ray diffraction and electron microscopy, interest in modulated temperature-differential scanning calorimetry (MT-DSC) has grown these recent years. Several studies have tentatively related the nanocomposite structure to the cooperativity length [23–30]. The method developed by Donth et al. [31,32] in the framework of the cooperative rearranging-regions (CRR) concept, introduced by Adam and Gibbs [33], makes it possible to estimate the cooperativity length from the mean temperature fluctuation associated with the glass transition, which is accessible thanks to MT-DSC. In a previous study on PLA/clay nanocomposites [34], we reported that exfoliated systems exhibit an increase in the CRR size in comparison to neat PLA, in agreement with the observations of Chen et al. on polystyrene/clay nanocomposites [23], whereas intercalation is characterized by a decrease in the CRR size. Calorimetric investigations also provide information regarding the mobility restrictions at the filler/matrix interface. These restrictions are characterized by a decrease of the heat-capacity step at the glass transition, revealing that a part of the amorphous phase does not mobilize. This interphase is named the *rigid amorphous fraction* ($X_{RAF\ filler}$) [35], in reference to the similar behavior commonly reported at the crystal/amorphous interface ($X_{RAF\ crystal}$). It is known that $X_{RAF\ crystal}$ strongly affects the macroscopic properties, such as mechanical or barrier properties [36,37]. Klonos et al. [38] showed that $X_{RAF\ filler}$ hinders thermal diffusivity, whereas $X_{RAF\ crystal}$ facilitates heat transport.

Thus, we used MT-DSC in this study to characterize PLA/lignin nanocomposites containing nanosheets (rGO), layer-like nanoclays (C30B), or nanotubes (MWCNT). This set of nanofillers was chosen in order to highlight possible shape and size effects influencing both the morphological and thermal properties of the hybrid nanocomposites. Qualitative filler dispersion was assessed from field-emission scanning-electron microscopy (FESEM) and transmission-electron microscopy (TEM). The thermal stability was evaluated from thermogravimetric analysis (TGA). Furthermore, cooperativity and the rigid amorphous fraction were estimated in amorphous and semi-crystalline samples. Since a number of the properties of PLA depend on its degree of crystallinity, the impact of the nanofiller choice on the crystallization kinetic was also reported.

2. Materials and Methods

2.1. Preparation of PLA/Lignin Hybrid Nanocomposites

Lignin was extracted from *Prosopis juliflora* (Sw.), collected from Gujarat, India. PLA-L105, which is named "PLLA" in the present paper, was purchased from Corbion®, Amsterdam, Netherlands with M_W = 148 kg mol^{-1}, L-enantiomeric purity of 99.5%, and with a melting temperature T_m = 180–200 °C. MWCNT were obtained from nanocyl (NANOCYL® NC7000), Sambreville, Belgium. C30B was made by Southern Clay Products®, Gonzales,

Texas, USA. rGO was synthesized using a previously reported procedure [39]. Graphite powder, $KMnO_4$, $NaNO_3$, H_2SO_4, and H_2O_2 (30%) were obtained from Merck®, Mumbai, India.

The components were mixed in chloroform using a probe sonicator. For each composition, 1 wt% of lignin/chloroform mixture and 1 wt% of filler/chloroform (rGO, MWCNT, or C30B) was added into the PLLA/chloroform mixture. The sonicated mixture of PLLA/lignin/nanofiller was cast on a petri dish and dried in an air oven at 70 °C.

In this paper, the nanocomposites are named PLLA_lignin_*X*, with *X* being the filler. The respective weight percentages of lignin (*y*) and nanofiller (*z*) are indicated as (*y:z*). When nothing is mentioned, the ratio between lignin and nanofiller is (1:1).

2.2. Field-Emission Scanning-Electron Microscopy (FESEM) and Transmission-Electron Microscopy (TEM)

The fracture-surface morphology was taken at 1 kV with the help of a Zeiss®, Marly le Roi, France, Gemini LEO 1530 apparatus at 60 kV. The samples were cryo-fractured and dried, and then the fracture surface was coated with a thin film of carbon (about 20–30 nm thickness) before performing the FESEM analysis.

TEM micrographs of the samples were taken using a Jeol JEM-2100®, Tokyo, Japan transmission-electron microscope with an accelerating voltage of 200 keV. Ultrathin sections of bulk specimens (about 100 nm in thickness) were obtained by crosscutting with an ultramicrotome fitted with a diamond knife.

2.3. Thermogravimetric Analysis (TGA)

Thermogravimetric analyses (TGA) were carried out using a TGA Discovery instrument from TA Instruments®, Guyancourt, France. The analyses were carried out under nitrogen atmosphere at 25 mL min^{-1} flow rate, in the temperature range of 30–800 °C and a scanning rate of 10 K min^{-1} on 5–10 mg samples.

2.4. Modulated Temperature-Differential Scanning Calorimetry (MT-DSC)

MT-DSC experiments were conducted on a DSC Q100 and DSC Q2000 from TA Instruments®, Guyancourt, France, coupled with a refrigerated cooling system. The experiments were conducted under nitrogen atmosphere at 50 mL min^{-1} flow rate. The samples were positioned in Tzero® standard aluminum pans. Baseline correction and cell-capacitance control were done using standard Tzero® technology. To calibrate the temperature and energy, a standard sample of Indium (T_m = 156.60 °C and ΔH_m = 28.38 J g^{-1}) was used. The calibration of the specific heat capacity was carried out using sapphire as a reference. Before the calorimetric investigations, the samples (about 5 mg) were placed in a desiccator under P_2O_5 and stored under a dehumidified atmosphere for at least one week.

To compare the crystallization kinetics between materials, the samples were first melted to erase the thermal history and optimize the thermal contact between the sample and the crucible. Then, the samples were cooled to 0 °C at 50 K min^{-1}. A heating scan was subsequently performed from 0 °C to 200 °C in heat-only conditions (oscillation amplitude of ±0.318 °C, oscillation period of 60 s, and heating rate of 2 K min^{-1}). These conditions prevent cooling in the modulation period, as the instantaneous heating rate is never negative. They are recommended for analyzing crystallization and melting events without the biases caused by melt-recrystallization processes [40].

Glass-transition-characteristic parameters and CRR size were obtained by applying heat–cool-modulation parameters (oscillation amplitude of ±2.5 °C, oscillation period of 100 s, and a heating rate equal to 1 K min^{-1}) on amorphous and semi-crystalline samples. These conditions respect the minimum number of modulation steps needed to investigate the glass transition, and were previously shown to be efficient for the study of PLA nanocomposites [34]. Amorphization was done using a Perkin Elmer®, Villebon-sur-Yvette, France, DSC8500 apparatus. The samples were cooled down from the melt to −50 °C at 300 K min^{-1}. Then, a first MT-DSC heat-cool scan was performed from 0 to 105 °C, i.e., until each sample reached its maximum crystallization extent, with the glass transition

being recorded at about 60 °C and the cold crystallization proceeding between 80 and 100 °C. In a second step, each sample was cooled to 0 °C at 50 K min^{-1} before being heated again to 105 °C in heat–cool conditions.

2.5. Cooperative Rearranging Regions (CRR)

The complete deconvolution procedure suggested by Reading [40] was applied, giving access to MT-DSC signals, with C' and C'' being the in-phase and the out-of-phase components of C^*, the complex heat capacity, respectively. More details regarding phase-lag correction and heat-capacity estimation can be found in [41]. The number of relaxing structural units per CRR, N_α, was estimated according to [32]:

$$ N_\alpha = \frac{N_A \left(\frac{1}{Cp'_{\text{glass (T\alpha)}}} - \frac{1}{Cp'_{\text{liquid (T\alpha)}}} \right) k_B \, T_\alpha^2}{M_0 \, (\delta T)^2} \tag{1} $$

where T_α is the dynamic glass-transition temperature, k_B the Boltzmann constant, Cp the heat capacity at constant pressure, M_0 the molar mass of one structural unit (one repeating unit in the present case, i.e., M_0 = 72 g mol^{-1}), N_A the Avogadro number, and δT the mean temperature fluctuation related to the glass-transition temperature of an average CRR. T_α is defined as the maximum of C'' Gaussian fit when δT is its standard deviation. Cp, $_{\text{glass (T\alpha)}}$ and Cp, $_{\text{liquid (T\alpha)}}$ are determined by prolonging C' glass and liquid lines to T_α.

3. Results and Discussion

The main morphological features associated with the dispersion of lignin and nanofillers into the PLLA matrix are shown in Figure 1, based on electron-microscopy analyses on PLLA_Lignin_MWCNT nanocomposites. One can observe the successful incorporation of lignin and nanofiller, appearing as light domains and white filaments, respectively, in the dark-colored PLLA matrix of the FESEM image, which is confirmed by the TEM image. The TEM micrograph shows the presence of MWCNT distributed homogeneously over lignin exhibiting good interaction between them. Lignin exhibits a highly complex chemical structure, in which several chemical functions can contribute to interfacial interactions, not only by the formation of hydrogen bonds through hydroxyl groups, but also by favoring secondary van der Waals interactions via phenyl and carbonyl groups, with the latter being particularly compatible with PLLA ester groups [42].
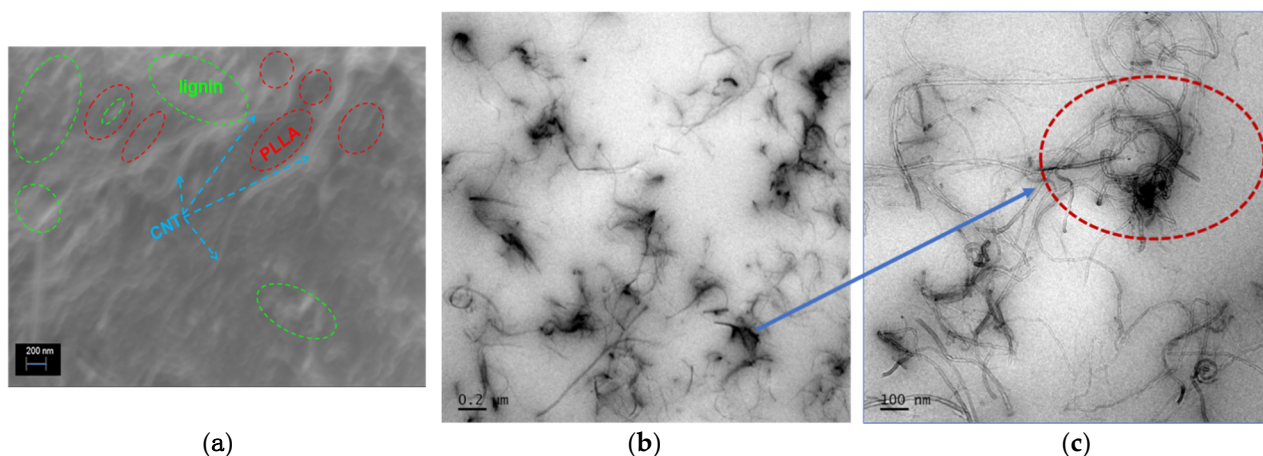

(a)   (b)   (c)

Figure 1. (**a**) FESEM image of PLLA_Lignin_MWCNT. PLLA matrix is indicated in red, and the areas containing lignin are shown in green. Blue arrows point at filament shapes, which are characteristic of MWCNT, (**b**,**c**) TEM images of PLLA_Lignin_MWCNT.

Figures 2 and 3 show the evolution of the weight percent as a function of temperature in PLLA_Lignin and hybrid nanocomposites, depending on the nanofiller nature (Figure 2)

and on the lignin/nanofiller ratio (Figure 3). Data regarding neat PLLA and neat lignin were also added in Figures 2 and 3, respectively. The degradation of neat lignin occurs in three stages, named the drying stage, the fast-degradation stage, and the slow-degradation stage by Ma et al. [43]. The degradation of PLA-based materials occurs in two steps: The weight loss corresponding to the temperature range 100–170 °C for all samples might be due to the presence of water, and the major weight loss observed in the range 280–395 °C might be due to the complete degradation of the matrix. Temperatures $T_{w\%}$ associated with representative mass-loss percentage $w\%$ are given in Table 1, with w = {5; 10; 50; 90; 95}.
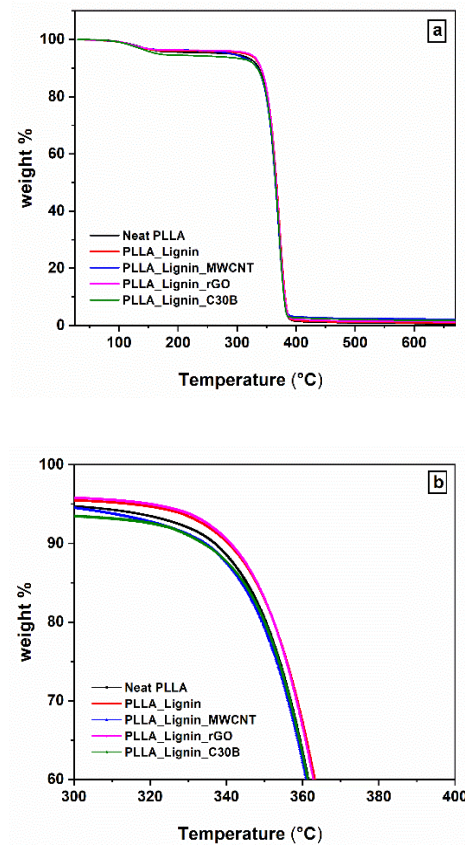

Figure 2. TGA profiles for neat PLLA, PLLA with additive, and nanocomposites. Influence of the filler choice: (**a**) global profile (**b**) focus on the onset of the main degradation step.
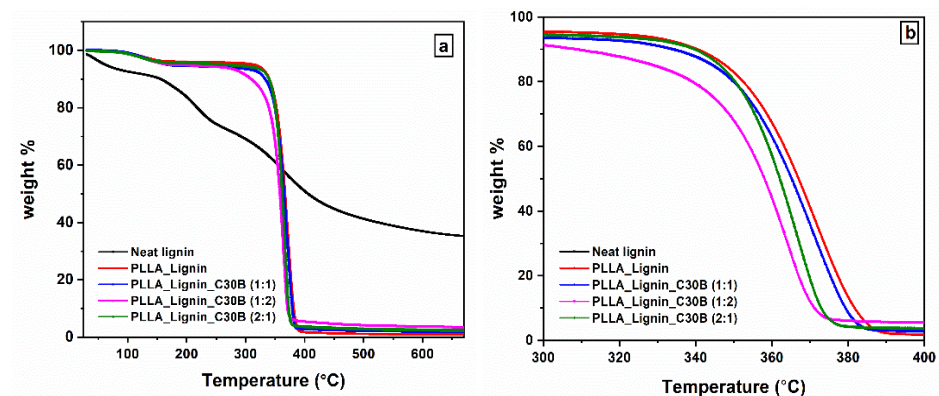

Figure 3. TGA profiles for PLLA with additive and nanocomposites. Influence of the lignin/filler ratio: (**a**) global profile (the TGA profile of lignin is added) (**b**) focus on the main degradation step.

Table 1. TGA and MT-DSC heat-only extracted parameters.

	TGA					MT–DSC			
	Temperatures Corresponding to % of Weight Loss (°C)					Heat Capacity Step ΔCp (J g^{-1} K^{-1}), Glass-Transition Temperature T_g (°C), Enthalpy of Cold–Crystallization ΔH_c (J g^{-1}), Degree of Crystallinity X_c (%)			
	$T_{5\%}$	$T_{10\%}$	$T_{50\%}$	$T_{90\%}$	$T_{95\%}$	ΔCp	T_g	ΔH_c	X_c *
neat PLLA	289	337	365	380	383	0.21	53.5	16	41
PLLA_Lignin	315	340	367	381	385	0.42	52.5	33	18
PLLA_Lignin_MWCNT	291	334	365	380	383	0.14	54.0	10	43
PLLA_Lignin_rGO	321	341	366	381	385	0.38	55.0	31	23
PLLA_Lignin_C30B (1:1)	166	334	365	379	382	0.43	56.5	30	23
PLLA_Lignin_C30B (1:2)	205	309	358	371	437	0.38	56.5	23	28
PLLA_Lignin_C30B (2:1)	270	340	362	373	377	0.42	56.5	29	21

* Uncertainties regarding X_c are ±2% from data reproducibility.

The $T_{5\%}$ values are dispersed because of slight variations regarding the water content in the samples. $T_{10\%}$ seems to be the most significant temperature at which to compare the thermal stability among nanocomposites, since it corresponds to the beginning of the matrix-degradation step (Figures 2b and 3b). First, the addition of lignin seems to slightly improve the thermal stability, as expected [44]. Nanocomposites for which the lignin/nanofiller ratio is (1:1) show small differences in their TGA profile. Some are consistent with previous results from the literature [45,46], e.g., rGO improves the thermal stability, whereas MWCNT induces the opposite effect. On the other hand, our results show accelerated degradation with the addition of C30B in contrast to the reported stabilizing effects [47]. The antagonist actions of both lignin and C30B are highlighted by modifying their ratio. $T_{10\%}$ shifts to higher values in PLLA_Lignin_C30B (2:1) but severely drops in PLLA_Lignin_C30B (1:2).

$T_{50\%}$, $T_{90\%}$, and $T_{95\%}$ are globally homogenous among materials, with the exception of PLLA_Lignin_C30B (2:1) and PLLA_Lignin_C30B (1:2). Both exhibit lower values of $T_{50\%}$ and $T_{90\%}$ compared to other systems, which is more surprising for PLLA_Lignin_C30B (2:1). We may assume that lignin, partly degraded, loses its stabilizing effect at these advanced stages of pyrolysis. $T_{95\%}$ is curiously high in PLLA_Lignin_C30B (1:2). However, this result might be influenced by the nanofiller content that does not degrade, which may hinder the release of gases.

Figure 4 gives the evolution of the MT-DSC average heat flow as a function of the temperature for all the samples, consecutive to cooling from the melt at 50 K min^{-1}. The classical behavior obtained for neat PLLA was observed as follows: a heat-flow step of around 55–60 °C, corresponding to the glass transition; an exothermic peak with a maximum at around 80 °C, corresponding to the cold crystallization; and an endothermic peak at around 170 °C, indicating the melting temperature. The addition of lignin brought about a remarkable change in the thermal behavior of the PLLA. Indeed, we observed that the amplitude of the heat-capacity step ΔCp at the glass transition and the enthalpy of cold crystallization ΔH_c were increased when the glass transition temperature T_g shifted to lower temperatures. These changes are the signature of a greater amorphization during cooling. The degree of crystallinity X_c, calculated according to Equation (2) and given in Table 1, confirms that the addition of lignin retards the PLLA crystallization.

$$X_C = \frac{\Delta H_f - \Sigma \Delta H_c}{\Delta H_f^\circ} \qquad (2)$$

where ΔH_f is the enthalpy of melting and ΔH_f° is the enthalpy of melting of 100% crystalline PLLA, which is considered to be equal to 93 J/g [48]. ΔH_c and ΔH_f were normalized to the mass of PLLA. The same normalization was applied to ΔCp (see Table 1).
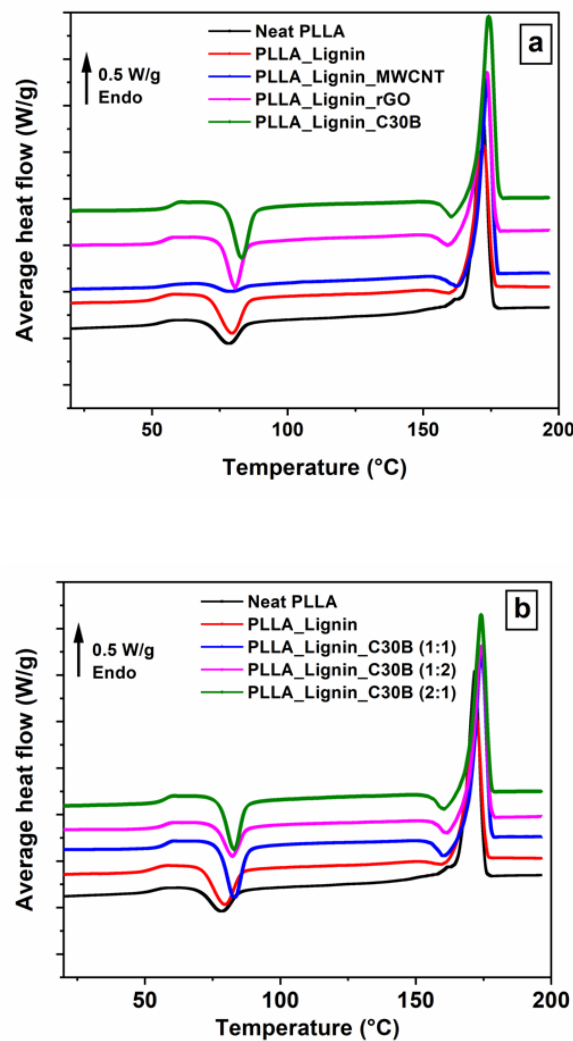
Figure 4. MT-DSC heat-only average heat flow signals: (**a**) influence of the filler choice; (**b**) influence of the lignin/filler ratio.

The results presented in Figure 4a and Table 1 highlight that only PLLA_Lignin_MWCNT crystallized more than neat PLLA under cooling from the melt. According to Hu et al. [46], carbon nanotubes are more efficient nucleating agents than rGO. Barrau et al. [49] proposed that the high specific surface of carbon nanotubes implies a large number of nucleation sites. Therefore, the crystallization rate, and consequently X_c, can be adjusted according to the choice of the filler. The results obtained for PLLA_Lignin_C30B show that additional control can be managed by modifying the filler/lignin ratio. This is interesting for industrial production, for which the cooling rate is not easily adjustable.

One can assume that lignin creates specific interactions with both the matrix and nanofillers, which could differ in nature, size, or content, depending on the nanofillers. The idea behind the calculation of the CRR size is to use the glass-transition calorimetric response as a fingerprint of the intermolecular architecture. To evaluate the impact of lignin and nanofillers properly, it is mandatory to investigate amorphous samples. Differences are observed regarding ΔCp, T_α, and ΔT, impacting the CRR size. The results are presented in Table 2 for all materials.

Table 2. Rigid amorphous fraction and crystalline-phase contents, as well as the characteristic amorphous-phase parameters extracted from the C' and C'' signals (ΔCp, T_α, and ΔT) that were used for the CRR-size calculation.

	Amorphous				Semi-crystalline					
	T_α (°C)	ΔT (°C)	ΔCp (J g^{-1} K^{-1})	N_α	T_α (°C)	ΔT (°C)	ΔCp (J g^{-1} K^{-1})	X_c * (%)	$X_{RAF\ crystal}$ ** (%)	N_α
neat PLLA	58.5	2.70	0.54	338	67.0	4.3	0.13	32	45	139
PLLA_Lignin	58.2	2.75	0.53	318	64.0	4.6	0.15	33	39	120
PLLA_Lignin_MWCNT	58.8	2.63	0.57	368	64.6	5.0	0.17	30	39	106
PLLA_Lignin_rGO	58.4	2.70	0.60	364	65.0	6.4	0.16	33	40	67
PLLA_Lignin_C30B (1:1)	59.2	2.68	0.54	346	67.2	4.9	0.18	31	35	105
PLLA_Lignin_C30B (1:2)	59.2	2.63	0.56	365	67.2	5.35	0.16	31	39	93
PLLA_Lignin_C30B (2:1)	59.6	2.40	0.58	458	65.6	4.8	0.19	29	40	119

* Uncertainties regarding X_c are $\pm 2\%$ from data reproducibility. ** Uncertainties regarding $X_{RAF\ crystal}$ are $\pm 5\%$ from data reproducibility.

Figure 5 and Table 2 show that the hybrid nanocomposites exhibit a slight increase of N_α and ΔCp. Classically reported effects of nanofillers on the calorimetric response at the glass transition are a decrease of ΔCp, attributed to the existence of $X_{RAF\ filler}$ [35], and a decrease of N_α [34], which is a consequence of mobility restrictions likely induced by $X_{RAF\ filler}$; both effects are in contradiction with our results. Equation (3), in which $\Delta Cp°$ is ΔCp of neat amorphous PLLA, is not valid in our case, as it leads to negative values for $X_{RAF\ filler}$.

$$X_{RAF\ filler} = 1 - \frac{\Delta Cp}{\Delta Cp°} \tag{3}$$

To explain the increase of ΔCp and N_α, we assumed a successful exfoliation [34], which favored intermolecular interactions without generating $X_{RAF\ filler}$, i.e., $X_{RAF\ filler}$ was equal to zero. Recently, Szymoniak et al. also reported an increase of ΔCp in epoxy-based nanocomposites [50], reaching an optimum before falling with the increase of the filler content, probably due to the competition existing between the creation of interactions and the mobility restrictions. According to our results, N_α is equal to 458 in PLLA_Lignin_C30B (2:1). Figure 6 shows C' and C'' signals for this system and PLLA_Lignin_C30B (1:1) for comparison. Such an increase in N_α in comparison with neat PLLA exceeded our expectations. We assume that this characterizes the role of lignin as an interaction promoter in hybrid nanocomposites.
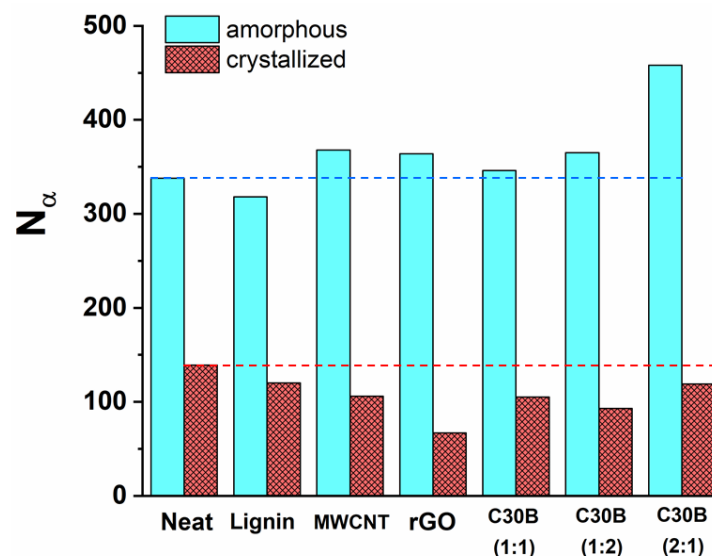
Figure 5. Number of relaxing units per CRR in amorphous and semi-crystalline PLLA and nanocomposites. Dashed lines are a guide, showing N_α for amorphous neat PLLA.
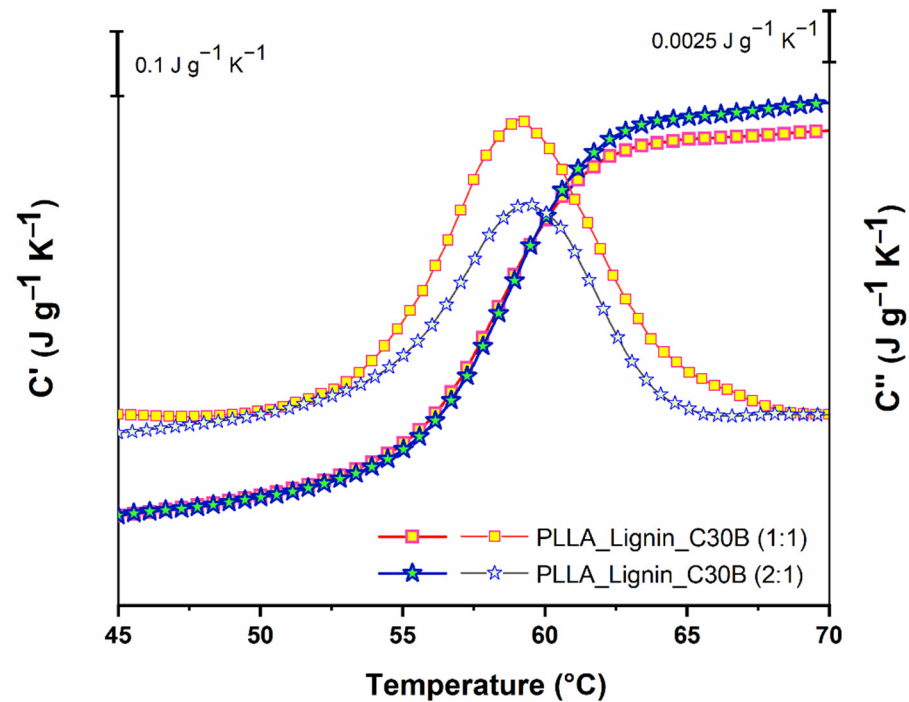
Figure 6. In-phase C' and out-of-phase C'' components of C^*, the complex heat capacity for PLLA_Lignin_C30B (1:1) and PLLA_Lignin_C30B (2:1) as a function of temperature from the MT-DSC heat-cool protocol: C' appears as a step and C'' as a peak. The thick markers and lines are used to plot C', whereas thin markers and lines refer to C''.

These considerations do not extend beyond amorphous systems. In semi-crystalline nanocomposites, the mobility criteria are strongly affected, and the response observed for amorphous systems is usually not reproduced. This is particularly obvious when high values of $X_{RAF\ crystal}$ are obtained, leading to a huge decrease in CRR size [34]. Therefore, we investigated the cooperativity in semi-crystalline nanocomposites annealed in conditions helping to grow $X_{RAF\ crystal}$ at a low temperature from the glassy state [51]. The results are given in Table 2. X_{RAF}, i.e., the total amount of rigid amorphous fraction in the investigated material is calculated according to Equation (4). $X_{RAF\ crystal}$ is obtained by subtracting $X_{RAF\ filler}$ from X_{RAF}. Because $X_{RAF\ filler}$ is null, $X_{RAF\ crystal}$ is simply equal to X_{RAF}.

$$X_{RAF} = X_{RAF\ crys} = 1 - \frac{\Delta Cp}{\Delta Cp^\circ} - X_c \tag{4}$$

First, N_α decreased from about 340 to 140 by annealing neat PLLA, as expected. X_c and $X_{RAF\ crystal}$ were similar between samples, but N_α was the highest for neat PLLA. A comparison among PLLA_Lignin_C30B materials revealed that this decrease in the CRR size was not related to the lignin, but to the nanofiller. Finally, N_α depends on the nature of the nanofiller. It reached the lowest value of 67 for PLLA_Lignin_rGO. Considering that X_c and $X_{RAF\ crystal}$ are similar between samples, this could reasonably indicate that the crystalline morphology differs. It has already been reported that PLA-based nanocomposites containing rGO nanoflakes are characterized by very imperfect crystals in comparison to neat PLLA [45]. For equally high measurements of X_c and $X_{RAF\ crystal}$, a decrease in the long period, i.e., in the spacing between adjacent crystalline lamellae layers, will result in a more efficient propagation of the mobility restriction from the crystal to the mobile amorphous through the RAF. To summarize, the results obtained for amorphous nanocomposites confirm the role of lignin as a promoter of interfacial interactions because the calorimetric response is highly sensitive to intermolecular interactions. On the other hand, the mi-

crostructure and the morphology govern the glass-transition signature in semi-crystalline nanocomposites, which is consistent with previous observations [34,52].

The structural dependence of the CRR size is not systematically accompanied by similar variations in other relaxation parameters characteristic of the glass-transition dynamics. The kinetic fragility index, for example [53], which characterizes the degree of deviation from the Arrhenius-type temperature dependence of the relaxation time when approaching the glass transition during cooling, can show complex variations with cooperativity [54]. Hong et al. [55] separated the fragility into two terms, volume and energetic, with only the first being correlated with cooperativity. This volume term has been interpreted by Araujo et al. [56] as the contribution of interchain interactions to the relaxation motions. One may assume that the kinetic fragility increases, along with cooperativity, by adding lignin to PLLA nanocomposites, due to the increase of the volume term; however, further investigations are needed to validate this assumption. Indeed, various trends can be found in the literature regarding fragility variations with nanofiller inclusion [24,50,57–59], and it has been shown that cooperativity and fragility can evolve in opposition [60].

4. Conclusions

Calorimetric studies can provide information regarding both interactions and mobility restrictions at the filler/matrix interface of nanocomposites, which is helpful for completing the morphological diagnostic, often limited to the filler-dispersion evaluation. It emerged from our results that lignin is a promising additive for the design of PLLA-based nanocomposites. Even when added in low amounts, it promotes a homogeneous dispersion or exfoliation when creating weak interactions with both filler and matrix, and regularly increases the thermal stability. Interestingly, lignin is versatile regarding its impact on PLLA-crystallization kinetic, depending on the chosen added nanofiller, which is of tremendous relevance for the material design. Moreover, the possible association between lignin and several nanofillers, exhibiting different shape, size, and dimensionality, offers other ways of modulating the macroscopic properties, as observed from the difference in amorphous dynamics among semi-crystalline samples. It is worth noting that lignin is a macromolecule that can be abundantly extracted from biomass. Thus, this study might contribute to the valorization of lignin for sustainable development.

References

1. Badia, J.D.; Ribes-Greus, A. Mechanical recycling of polylactide, upgrading trends and combination of valorization techniques. *Eur. Polym. J.* **2016**, *84*, 22–39. [CrossRef]
2. Tsuji, H.; Yamamoto, S.; Okumura, A. Homo- and hetero-stereocomplexes of substituted poly(lactide)s as promising biodegradable crystallization–accelerating agents of poly(L–lactide). *J. Appl. Polym. Sci.* **2011**, *122*, 321–333. [CrossRef]
3. Bhardwaj, R.; Mohanty, A.K. Modification of brittle polylactide by novel hyperbranched polymer-based nanostructures. *Biomacromolecules* **2007**, *8*, 2476–2484. [CrossRef] [PubMed]
4. Azizi, S.; Azizi, M.; Sabetzadeh, M. The role of multiwalled carbon nanotubes in the mechanical, thermal, rheological, and electrical properties of PP/PLA/MWCNTs nanocomposites. *J. Compos. Sci.* **2019**, *3*, 64. [CrossRef]
5. Trifol, J.; Plackett, D.; Sillard, C.; Szabo, P.; Bras, J.; Daugaard, A.E. Hybrid poly(lactic acid)/nanocellulose/nanoclay composites with synergistically enhanced barrier properties and improved thermomechanical resistance. *Polym. Int.* **2016**, *65*, 988–995. [CrossRef]
6. Molinaro, S.; Romero, M.C.; Boaro, M.; Sensidoni, A.; Lagazio, C.; Morris, M.; Kerry, J. Effect of nanoclay-type and PLA optical purity on the characteristics of PLA–based nanocomposite films. *J. Food Eng.* **2013**, *117*, 113–123. [CrossRef]
7. Arriagada, P.; Palza, H.; Palma, P.; Flores, M.; Caviedes, P. Poly(lactic acid) composites based on graphene oxide particles with antibacterial behavior enhanced by electrical stimulus and biocompatibility. *J. Biomed. Mater. Res. A* **2018**, *106*, 1051–1060. [CrossRef]
8. Mina, M.F.; Beg, M.D.H.; Islam, M.R.; Nizam, A.; Alam, A.K.M.M.; Yunus, R.M. Structures and properties of injection-molded biodegradable poly(lactic acid) nanocomposites prepared with untreated and treated multiwalled carbon nanotubes. *Polym. Eng. Sci.* **2014**, *54*, 317–326. [CrossRef]
9. Doherty, W.O.; Mousavioun, P.; Fellows, C.M. Value–adding to cellulosic ethanol: Lignin polymers. *Ind. Crops Prod.* **2011**, *33*, 259–276. [CrossRef]
10. Chen, J.; Liu, C.; Wu, S.; Liang, J.; Lei, M. Enhancing the quality of bio–oil from catalytic pyrolysis of kraft black liquor lignin. *RSC Adv.* **2016**, *6*, 107970–107976. [CrossRef]
11. Ragauskas, A.J.; Beckham, G.T.; Biddy, M.J.; Chandra, R.; Chen, F.; Davis, M.F.; Davison, B.H.; Dixon, R.A.; Gilna, P.; Keller, M.; et al. Lignin valorization: Improving lignin processing in the biorefinery. *Science* **2014**, *344*, 1246843. [CrossRef] [PubMed]
12. Park, C.W.; Youe, W.J.; Han, S.Y.; Kim, Y.S.; Lee, S.H. Characteristics of carbon naonfibers produced from lignin/polyacrylonitrile (PAN)/kraft lignin–g–PAN copolymer blends electrospun nanofibers. *Holforschung* **2017**, *71*, 746–750. [CrossRef]
13. Baker, D.A.; Rials, T.G. Recent advance in low-cost carbon fiber manufacture from lignin. *J. Appl. Polym. Sci.* **2013**, *130*, 713–728. [CrossRef]
14. Spiridon, I.; Leluk, K.; Resmerita, A.M.; Darie, R.N. Evaluation of PLA–lignin bioplastics properties before and after accelerated weathering. *Compos. Part B Eng.* **2015**, *69*, 342–349. [CrossRef]
15. Sahoo, S.; Misra, M.; Mohanty, A.K. Enhanced properties of lignin–based biodegradable polymer composites using injection moulding process. *Compos. Part A Appl. S.* **2011**, *42*, 1710–1718. [CrossRef]
16. Chung, Y.-L.; Olsson, J.V.; Li, R.J.; Frank, C.W.; Waymouth, R.M.; Billington, S.L.; Sattely, E.S. A renewable lignin–lactide copolymer and application in biobased composites. *ACS Sustain. Chem. Eng.* **2013**, *1*, 1231–1238. [CrossRef]
17. Sun, Y.; Yang, L.; Lu, X.; He, C. Biodegradable and renewable poly(lactide)–lignin composites: Synthesis, interface and toughening mechanism. *J. Mater. Chem. A* **2015**, *3*, 3699–3709. [CrossRef]
18. Tanase-Opedal, M.; Espinosa, E.; Rodríguez, A.; Chinga-Carrasco, G. Lignin: A biopolymer from forestry biomass for biocomposites and 3D printing. *Materials* **2019**, *12*, 3006. [CrossRef]
19. Cauley, A.N.; Wilson, J.N. Functionalized lignin biomaterials for enhancing optical properties and cellular interactions of dyes. *Biomater. Sci.* **2017**, *5*, 2114–2121. [CrossRef]
20. Privas, E.; Leroux, F.; Navard, P. Preparation and properties of blends composed of lignosulfonated layered double hydroxide/plasticized starch and thermoplastics. *Carbohyd. Polym.* **2013**, *96*, 91–100. [CrossRef]
21. Chupin, L.; Charrier, B.; Pizzi, A.; Perdomo, A.; Charrier–El Bouhtoury, F. Study of thermal durability properties of tannin–lignosulfonate adhesives. *J. Therm. Anal. Calorim.* **2015**, *119*, 1577–1585. [CrossRef]
22. Graupner, N. Application of lignin as natural adhesion promoter in cotton fibre–reinforced poly(lactic acid) (PLA) composites. *J. Mater. Sci.* **2008**, *43*, 5222–5229. [CrossRef]
23. Chen, K.; Wilkie, C.A.; Vyazovkin, S. Nanoconfinement revealed in degradation and relaxation studies of two structurally different polystyrene–clay systems. *J. Phys. Chem. B* **2007**, *111*, 12685–12692. [CrossRef] [PubMed]
24. Saiter, A.; Couderc, H.; Grenet, J. Characterisation of structural relaxation phenomena in polymeric materials from thermal analysis investigations. *J. Therm. Anal. Cal.* **2007**, *88*, 483–488. [CrossRef]
25. Leszczynska, A.; Pielichowski, K. Application of thermal analysis methods for characterization of polymer/montmorillonite nanocomposites. *J. Therm. Anal. Calorim.* **2007**, *93*, 677–687. [CrossRef]
26. Greco, A.; Gennaro, R.; Rizzo, M. Glass transition and cooperative rearranging regions in amorphous thermoplastic nanocomposites. *Polym. Int.* **2012**, *61*, 1326–1333. [CrossRef]
27. Yousefzade, O.; Garmabi, H.; Puiggali, J. Cooperative rearranging region and dynamical heterogeneity of nanocomposites in poly(l-lactide) and functionalized carbon nanotubes systems. *Thermochim. Acta* **2018**, *667*, 35–41. [CrossRef]

28.   Khan, A.N.; Hayder, A.; Chaung, W.-T.; Hong, P.-D. Glass transition behavior of poly(trimethylene 2,6-naphthalate) in nanoclay confinement. *Polym. Sci. Ser. A* **2015**, *57*, 874–882. [CrossRef]

29.   Sharma, M.; Madras, G.; Bose, S. Cooperativity and structural relaxations in PVDF/PMMA blends in the presence of MWNTs: An assessment through SAXS and dielectric spectroscopy. *Macromolecules* **2014**, *47*, 1392–1402. [CrossRef]

30.   Patanair, B.; Thomas, S.; Abitha, V.K.; Saiter–Fourcin, A. Confinement effects at nanoscale in natural rubber composites: Influence on macroscopic properties. *J. App. Polym. Sci.* **2020**, *138*, 49838. [CrossRef]

31.   Donth, E. The size of cooperatively rearranging regions at the glass transition. *J. Non-Cryst. Solids* **1982**, *53*, 325–330. [CrossRef]

32.   Hempel, E.; Hempel, G.; Hensel, A.; Schick, C.; Donth, E. Characteristic length of dynamic glass transition near tg for a wide assortment of glass-forming substances. *J. Phys. Chem. B* **2000**, *104*, 2460–2466. [CrossRef]

33.   Adam, G.; Gibbs, J.H. On the temperature dependence of cooperative relaxation properties in glass–forming liquids. *J. Chem. Phys.* **1965**, *43*, 139. [CrossRef]

34.   Saiter, A.; Delpouve, N.; Dargent, E.; Oberhauser, W.; Conzatti, L.; Cicogna, F.; Passaglia, E. Probing the chain segment mobility at the interface of semi-crystalline polylactide/clay nanocomposites. *Eur. Polym. J.* **2016**, *78*, 274–289. [CrossRef]

35.   Wurm, A.; Ismail, M.; Kretzschmar, B.; Pospiech, D.; Schick, C. Retarded crystallization in polyamide/layered silicates nanocomposites caused by an immobilized interphase. *Macromolecules* **2010**, *43*, 1480–1487. [CrossRef]

36.   Aliotta, L.; Gazzano, M.; Lazzeri, A.; Righetti, M.C. Constrained amorphous interphase in poly(l-lactic acid): Estimation of the tensile elastic modulus. *ACS Omega* **2020**, *5*, 20890–20902. [CrossRef]

37.   Fernandes Nassar, S.; Guinault, A.; Delpouve, N.; Divry, V.; Ducruet, V.; Sollogoub, C.; Domenek, S. Multi-scale analysis of the impact of polylactide morphology on gas barrier properties. *Polymer* **2017**, *108*, 163–172. [CrossRef]

38.   Klonos, P.A.; Peoglos, V.; Bikiaris, D.N.; Kyritsis, A. Rigid amorphous fraction and thermal diffusivity in nanocomposites based on poly(l–lactic acid) filled with carbon nanotubes and graphene oxide. *J. Phys. Chem. C* **2020**, *124*, 5469–5479. [CrossRef]

39.   Akhina, H.; Gopinathan Nair, M.R.; Kalarikkal, N.; Pramoda, K.P.; Ru, T.H.; Kailas, L.; Thomas, S. Plasticized PVC graphene nanocomposites: Morphology, mechanical, and dynamic mechanical properties. *Polym. Eng. Sci.* **2017**, *58*, 858–865. [CrossRef]

40.   Lacey, A.A.; Price, D.M.; Reading, M. Theory and practice of modulated temperature differential scanning calorimetry. In *Modulated Temperature Differential Scanning Calorimetry*; Reading, M., Hourston, D.J., Eds.; Springer: Dordrecht, The Netherlands, 2006; Volume 6, pp. 1–81. [CrossRef]

41.   Varol, N.; Delpouve, N.; Araujo, S.; Domenek, S.; Guinault, A.; Golovchak, R.; Ingram, A.; Delbreilh, L.; Dargent, E. Amorphous rigidification and cooperativity drop in semi–crystalline plasticized polylactide. *Polymer* **2020**, *194*, 122373. [CrossRef]

42.   Dobircau, L.; Delpouve, N.; Herbinet, R.; Domenek, S.; Le Pluart, L.; Delbreilh, L.; Ducruet, V.; Dargent, E. Molecular mobility and physical ageing of plasticized poly(lactide). *Polym. Eng. Sci.* **2015**, *55*, 858–865. [CrossRef]

43.   Ma, Z.; Sun, Q.; Ye, J.; Yao, Q.; Zhao, C. Study on the thermal degradation behaviors and kinetics of alkali lignin for production of phenolic-rich bio-oil using TGA–FTIR and Py–GC/MS. *J. Anal. Appl. Pyrol.* **2016**, *117*, 116–124. [CrossRef]

44.   Gordobil, O.; Delucis, R.; Egüés, I.; Labidi, J. Kraft lignin as filler in PLA to improve ductility and thermal properties. *Ind. Crops Prod.* **2015**, *72*, 46–53. [CrossRef]

45.   Ferreira, W.H.; Andrade, C.T. The role of graphene on thermally induced shape memory properties of poly(lactic acid) extruded composites. *J. Therm. Anal. Calorim.* **2020**, 1–9. [CrossRef]

46.   Hu, C.; Li, Z.; Wang, Y.; Gao, J.; Dai, K.; Zheng, G.; Liu, C.; Shen, C.; Song, H.; Guo, Z. Comparative assessment of the strain-sensing behaviors of polylactic acid nanocomposites: Reduced graphene oxide or carbon nanotubes. *J. Mater. Chem. C* **2017**, *3*, 2318–2328. [CrossRef]

47.   Iturrondobeitia, M.; Okariz, A.; Guraya, T.; Zaldua, A.-M.; Ibarretxe, J. Influence of the processing parameters and composition on the thermal stability of PLA/nanoclay bio-nanocomposites. *J. Appl. Polym. Sci.* **2014**, *131*, 40747. [CrossRef]

48.   Fischer, E.W.; Sterzel, H.J.; Wegner, G. Investigation of the structure of solution grown crystals of lactide copolymers by means of chemical reactions. *Kolloid Z. Z. Polym.* **1973**, *251*, 980–990. [CrossRef]

49.   Barrau, S.; Vanmansart, C.; Moreau, M.; Addad, A.; Stoclet, G.; Lefebvre, J.-M.; Seguela, R. Crystallization behavior of carbon nanotube–polylactide nanocomposites. *Macromolecules* **2011**, *44*, 6496–6502. [CrossRef]

50.   Szymoniak, P.; Pauw, B.R.; Qu, X.; Schönhals, A. Competition of nanoparticle–induced mobilization and immobilization effects on segmental dynamics of an epoxy–based nanocomposite. *Soft Matter* **2020**, *16*, 5406–5421. [CrossRef]

51.   Delpouve, N.; Saiter–Fourcin, A.; Coiai, S.; Cicogna, F.; Spiniello, R.; Oberhauser, W.; Legnaioli, S.; Ishak, R.; Passaglia, E. Effects of organo-LDH dispersion on thermal stability, crystallinity and mechanical features of PLA. *Polymer* **2020**, *208*, 122952. [CrossRef]

52.   Klonos, P.; Terzopoulou, Z.; Koutsoumpis, S.; Zidropoulos, S.; Kripotou, S.; Papageorgiou, G.Z.; Bikiaris, D.N.; Kyritsis, A.; Pissis, P. Rigid amorphous fraction and segmental dynamics in nanocomposites based on poly(l-lactic acid) and nano-inclusions of 1-3D geometry studied by thermal and dielectric techniques. *Polymer* **2016**, *82*, 16–34. [CrossRef]

53.   Angell, C.A. Spectroscopy simulation and scattering, and the medium range order problem in glass. *J. Non-Cryst. Solids* **1985**, *73*, 1–17. [CrossRef]

54.   Delpouve, N.; Delbreilh, L.; Stoclet, G.; Saiter, A.; Dargent, E. Structural dependence of the molecular mobility in the amorphous fractions of polylactide. *Macromolecules* **2014**, *47*, 5186–5197. [CrossRef]

55.   Hong, L.; Novikov, V.N.; Sokolov, A.P. Is there a connection between fragility of glass forming systems and dynamic heterogeneity/cooperativity? *J. Non-Cryst. Solids* **2011**, *357*, 351–356. [CrossRef]

56. Araujo, S.; Batteux, B.; Li, W.; Butterfield, L.; Delpouve, N.; Esposito, A.; Tan, L.; Saiter, J.-M.; Negahban, M. A structural interpretation of the two components governing the kinetic fragility from the example of interpenetrated polymer networks. *J. Polym. Sci. Pol. Phys.* **2018**, *56*, 1393–1403. [CrossRef]
57. Laredo, E.; Grimau, M.; Bello, A.; Wu, D. Molecular dynamics and crystallization precursors in polylactide and poly(lactide)/CNT biocomposites in the insulating state. *Eur. Polym. J.* **2013**, *49*, 4008–4019. [CrossRef]
58. Sanusi, O.M.; Papadopoulos, L.; Klonos, P.A.; Terzopoulou, Z.; Hocine, N.A.; Benelfellah, A.; Papageorgiou, G.Z.; Kyritsis, A.; Bikiaris, D.N. Calorimetric and dielectric study of renewable poly(hexylene 2,5-furan-dicarboxylate)-based nanocomposites in situ filled with small amounts of graphene platelets and silica nanoparticles. *Polymers* **2020**, *12*, 1239. [CrossRef]
59. Crétois, R.; Delbreilh, L.; Dargent, E.; Follain, N.; Lebrun, L.; Saiter, J.-M. Dielectric relaxations in polyhydroxyalka-noates/organoclay nanocomposites. *Eur. Polym. J.* **2013**, *49*, 3434–3444. [CrossRef]
60. Sharma, M.; Madras, G.; Bose, S. Unusual fragility and cooperativity in glass–forming and crystalline PVDF/PMMA blends in the presence of multiwall carbon nanotubes. *Macromolecules* **2015**, *48*, 2740–2750. [CrossRef]